Materiales de Construcción
Vol. 73, Issue 349, January-March 2023, e304
ISSN-L: 0465-2746
https://doi.org/10.3989/mc.2023.301422

Effects of the mineralogical composition and particle size distribution of ladle furnace slag as a cement/fine aggregate replacement in concrete

P. Araos✉, T. Montaño, S. Valls, M. Barra, D. Aponte

Department of Civil and Environmental Engineering, Universitat Politècnica de Catalunya BarcelonaTech (Barcelona, Spain)
✉: paulo.sebastian.araos@upc.edu

Received 31 August 2022
Accepted 06 December 2022
Available on line 06 March 2023

ABSTRACT: Ladle furnace slag (LFS) shows excellent potential for valorization. Despite this, landfills are typically its final destination, mainly because of technological barriers in its valorization process. This work examines the potential use of LFS as a partial cement/fine aggregate replacement, focusing on the effects of LFS composition and particle size distribution on concrete physico–mechanical properties. Chemical/mineralogical characterization of raw/hydrated samples, fresh-/hardened-state concrete properties, and volumetric instability tests were evaluated. Our results show reduced mechanical performance with LFS replacement, reaching compressive strength values of 32–42 MPa after 28 days. LFS mineralogical characterization reveals the absence of free CaO and the presence of periclase with its hydration/carbonation products. Therefore, the weathering/maturity process mainly affects free CaO. Furthermore, the observed volumetric instability issues were within the Code on Structural Concrete (Spanish abbreviation:-EHE) established limits (0.04%), suggesting that the remaining periclase could be responsible for this expansive behavior.

KEY WORDS: Concrete; Ladle furnace slag; Mechanical properties; Volumetric instability; Microstructure.

Citation/Citar como: Araos, P.; Montaño, T.; Valls, S.; Barra, M.; Aponte, D. (2023) Effects of the mineralogical composition and particle size distribution of ladle furnace slag as a cement/fine aggregate replacement in concrete. Mater. Construcc. 73 [349], e304. https://doi.org/10.3989/mc.2023.301422.

RESUMEN: *Efecto de la composición mineralógica y granulometría de la escoria blanca de acería como un reemplazo de cemento/árido fino en hormigón*. La escoria blanca de acería (LFS) presenta potencial para ser valorizada. Sin embargo, su destino es ser depositada en vertedero, debido a barreras tecnológicas en su proceso de valorización. Este trabajo explora el potencial uso de LFS como reemplazo parcial de cemento/árido fino, enfocándose en los efectos de la composición y granulometría de LFS sobre propiedades físico-mecánicas. Se evalúa la composición química/mineralógica (muestras anhidras/hidratadas), propiedades en estado fresco/endurecido y ensayos de inestabilidad volumétrica en hormigón. Los resultados muestran un menor desempeño mecánico con el reemplazo de LFS, alcanzando 32-42 MPa de resistencia a compresión (28 días). La caracterización mineralógica de LFS revela la ausencia de CaO-libre y presencia de periclasa con sus productos de hidratación/carbonatación. Por lo tanto, el proceso de meteorización/maduración afecta principalmente a la CaO-libre. Además, la inestabilidad volumétrica observada se encuentra dentro de los límites establecidos por la EHE (0,04%), donde la periclasa remanente podría ser la responsable de este comportamiento expansivo.

PALABRAS CLAVE: Hormigón; Escoria blanca de acería; Propiedades mecánicas; Inestabilidad volumétrica; Microestructura.

1. INTRODUCTION

Ongoing industrial progress and increasing social–environmental concern will force the construction industry to adapt and modify from a linear-type economy (take–make–dispose) to a circular one. Nowadays, many industrial wastes are not valorized and are ultimately deposited in landfills as residues rather than contributing to an industry that is more oriented toward a circular economy. This will soon change owing to an inevitable shift toward more environmentally friendly processes.

Cement and concrete industries are important sources of greenhouse gas emissions and intensive natural resource consumption. Cement production is estimated to be responsible for approximately 5–8% of total CO_2 emissions (1). Several improvements have been introduced to mitigate these negative externalities, including complete modernization and optimization of its industrial processes, the use of alternative fuels, valorizing industrial residues as partial clinker replacements, and the use of supplementary cementitious materials (SCM) to reduce cement consumption (1-4). Another major actor in the construction sector, the steelmaking industry, exhibits significant production growth and will continue to rise in the coming decades (5). Production trends lean toward the electric arc furnace (EAF) route because of the possibility of reusing scrap (5). This route generates two main residues: EAF slag and ladle furnace slag (LFS). LFS is an attractive residue for valorization because of its physical properties, chemical–mineralogical composition, and affinity with cement-based materials (6).

However, owing to technological barriers in its valorization process (low cementing activity and volume instability problems), LFS's ultimate fate is deposition in landfills (6). These challenges arise mainly because of LFS's characteristic mineralogical composition which, in turn, results from the EAF route in the steelmaking process. During the hydration process, reactive calcium–aluminum phases experience a series of metastable phase transformations (7) or delayed hydration inside the rigid cement matrix (8) that can contribute to instability problems and low strength. Additionally, free CaO and periclase, typical phases found in LFS if not treated properly in the weathering/maturity stages, are key in generating instability problems. These may include expansive reactions when these phases are hydrated/carbonated inside a rigid matrix on cement-based materials (9-12).

The technical literature reveals high variability in LFS mineralogical composition, especially in the presence of free CaO and periclase. In some cases, free CaO is reported to be present (13-16) in the slag. However, several other studies observed the absence of this phase in the final mineralogical composition of LFS (10, 17-20). The reasons for the absence of free CaO are not always clear, but could be the cooling treatments in steelworks plants which are part of the normal slag management process (weathering). Alternatively, it could be due to a specific process in the recovery plant used to eliminate problematic phases present in the slag, typically by spraying water (maturity). The consumption of free CaO in the weathering/maturity process is owed to its rapid reaction kinetics, forming more stable phases such as portlandite and calcite and reducing potential expansive behavior. However, the presence of periclase in LFS's final mineralogical composition is more consistent. Additionally, the previously mentioned treatments for eliminating problematic expansive phases (weathering/maturity) have little or no impact on periclase owing to its slower reaction kinetics. Finally, periclase is not totally transformed into more stable phases. Instead, it remains in raw slag and could be the main phase responsible for volumetric instability issues.

So far, several works have studied the use of LFS as an SCM but mainly in a cement paste or a mortar matrix. Focusing mostly on studying physico–mechanical properties, durability, and volumetric instability, contradictory results have been obtained (8, 14, 19). Performance differences are associated primarily with the variability of mineralogical composition and particle size distribution (PSD) between the different LFSs. In addition, other studies have concluded that adding LFS as a replacement for an inert filler (limestone) in a concrete-type matrix could improve fresh-/hardened-state properties such as lower requirements for superplasticizer addition (21), increased mechanical performance at later ages (21, 22), and enhanced durability against chloride and carbonation penetration (21, 23). Only a few studies have dealt with the use of LFS solely as an SCM in a concrete-type matrix and exhibited promising results. For example, when using LFS in self-compacting concrete (up to 25 wt% cement replacement), an improvement was found in fresh-state properties and mechanical performance (24). Moreover, in (25, 26), the authors used an interesting approach to produce dual replacement of cement and aggregates. They used a mixture of two types of slags with different PSDs: EAFS with a broad PSD and higher maximum particle size as an aggregate replacement and LFS with a smaller maximum particle size as a cement replacement. They concluded that using a mixture of different types of slags for dual aggregate/cement replacement yields acceptable fresh-/hardened-state properties.

To our knowledge, the present study is one of only a few works that study the effects of using a single material, LFS, to accomplish dual cement/fine aggregate replacement in a concrete-type matrix. The main objective of this study is to verify the effects of LFS's chemical/mineralogical composition and particle size distribution on physico–mechanical

properties and volumetric instability in concrete. Finally, we correlate the microstructural changes in the concrete matrix with macrostructural performance.

2. MATERIALS AND METHODS

The materials used in this study were Portland cement type I 52.5 R (CEM) prepared according to UNE-EN 197-1 (27), tap water (W), and limestone aggregate with three different particle size distributions (PSD) identified as coarse (C-Ag), medium (M-Ag), and fine (F-Ag) aggregate. Table 1 summarizes the aggregates' physical properties and chemical composition as determined by X-ray fluorescence. In addition, a superplasticizer (Masterglenium UG 1323, BASF) was used to ensure workability of the concrete samples.

Two types of slag were used, both from the same plant but from different batches subjected to a six-month weathering process. The first was a coarse slag (labeled LFS-G) with a PSD ranging over 0–2 mm as tested according to UNE-EN 933-1 (28). The second (labeled LFS-F) consisted of a material whose particles were all less than 0.125 mm in size; the finer PSD was achieved by grinding the raw slag in a ball mill. The density values of LFS-G and LFS-F were 2.82 g/cm^3 and 2.73 g/cm^3, respectively, as determined according to UNE 80103:2013 (29). The PSDs of all aggregate and LFS materials used in this work are shown in Figure 1.

Concrete mix proportioning was calculated using the Bolomey method with a cement content of 377.78 kg/m^3. A water-to-cement ratio (W/C) of 0.45 was selected. Finally, the addition of 1.2 wt% of superplasticizer (Super) relative to the cement content was chosen to ensure the workability of the control sample.

To study the effects of LFS as a dual cement/fine aggregate replacement, concrete samples

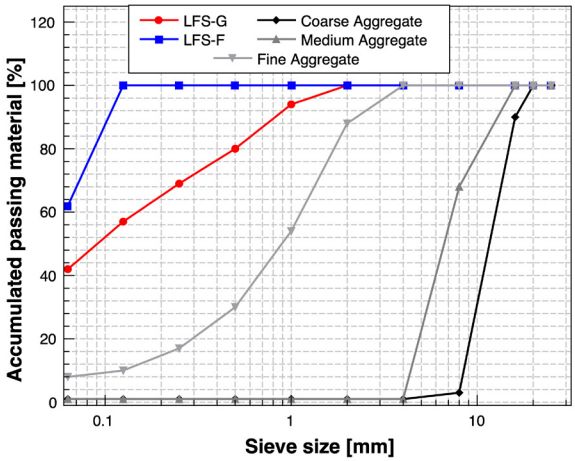

FIGURE 1. Aggregate and LFS particle size distributions.

were made using replacements of 12 wt% of fine aggregates and 18 wt% of cement, using only LFS-G as the dual replacement material (labeled HG). A single, 24 wt% cement replacement was made for the LFS-F concrete sample (labeled HF). Table 2 summarizes the mix proportioning for the samples used while Figure 2 compares the final mix designs. All the experimental mix design curves exhibited very similar behavior to the Bolomey method curve (labeled as Bolomey). The concrete control sample without any slag addition is labeled as HC.

A complete study of chemical and mineralogical composition was conducted to characterize the raw materials used in the present work and to examine the evolution of the concrete microstructure with LFS cement/fine aggregate replacement. This was achieved using X-ray fluorescence (XRF), Fourier transform infrared spectroscopy (FTIR), and X-ray diffraction (XRD) techniques.

The chemical composition of the raw materials as determined by XRF (Philips PW2400 Spectrometer) is shown in Table 3. All samples presented a

TABLE 1. Physical and chemical properties of the aggregates used.

Material	Density [g/cm^3]	Water absorption [%]	Composition [wt% for all aggregates]						
			CaO	Al_2O_3	SiO_2	MgO	Fe_2O_3	∑ others	LOI
C-Ag	2.71	0.58	54.25	1.14	0.85	0.6	0.19	0.19	42.78
M-Ag	2.48	0.68							
F-Ag	2.73	1.74							

TABLE 2. Concrete mix sample proportioning (in kg/m^3).

Sample	CEM	W	C-Ag	M-Ag	F-Ag	LFS		Super
						CEM replacement	F-Ag replacement	
HC	377.8	170	552.9	550.9	762.5	-	-	4.5
HG	303.6	170	552.9	551.2	673.1	69.3	95.8	4.5
HF	273.6	170	553.0	551.2	761.5	91.4	-	4.5

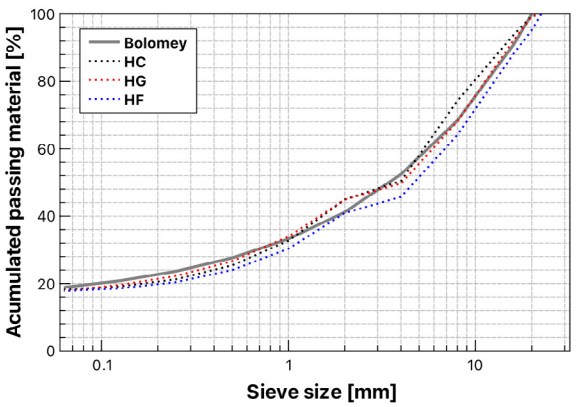

FIGURE 2. Comparison of the Bolomey curve and the resultant mix design control, LFS-G, and LFS-F samples (HC, HG, and HF, respectively).

similar chemical composition rich in Ca and Si, followed (in order of mass percent) by Fe, Al, and Mg, which represented more than 92% of the total mass in the cement and 88% in both slags. In the case of the LFSs, these elements were derived from materials added at the refinement stage of the EAF route (scrap and fluxes, among others) and exhibit Ca/Si and Si/Al ratios lower than those in the cement sample (see Table 3). This combination of chemical composition and oxide ratios could lead to the formation of silicates/aluminates of calcium and magnesium phases. This is described below in the mineralogical composition characterization section. However, due to the higher content of Al and Mg, the resulting phases differ from those in cement and show less reactive hydraulic activity. It is important to highlight the iron oxide content difference between the slags; this could be related to EAFS contamination as traces of EAFS persist into the refinement stage of the steelmaking process. Finally, S and Mn were present in minor amounts along with traces of other elements. According to the literature (30-32), the observed chemical composition was within the expected ranges for this type of slag.

Attenuated total reflectance FTIR (ATR-FTIR) scans were acquired using Perkin Elmer Frontier equipment at room temperature with Spectrum software. Each ATR-FTIR spectrum was acquired using 16 scans at a spectral resolution of 4 cm^{-1} over a range of 4000–400 cm^{-1}. XRD scans were obtained using a Bruker D8-A25 powder diffractometer with Cu Kα radiation (λ =1.5406 Å for Kα1 and λ =1.5445 Å for Kα2, I1/I2= 1.89) 40 kV and 40 mA, a Ni chromator to filter out Cu Kb radiation, and a Lynxeye (PSD) detector. The scans were performed between 5°2θ and 55°2θ with a 0.019° step size and a counting time of 0.8 s per step. The qualitative identification of all phases was performed with Bruker Diffracc. EVA v4.2.1 software using the PDF-2 and COD databases.

Cement pastes with similar proportions to the concrete samples were prepared to study microstructure evolution. The specimen hydration process was stopped using the solvent exchange method. Next, the samples were pulverized to a particle size below 0.063 mm; then they were homogenized, after which they were ready for use in the aforementioned techniques. ATR-FTIR measurements were acquired after 7, 28, and 60 curing days and for XRD after 7, 28, 60, and 150 curing days. For the samples subjected to two different curing environments, only the 150-day measurements were performed, as described below.

To study the effects of using LFS as a cement/fine aggregate replacement at the macroscopic level, fresh-/hardened-state properties were measured using the slump test according to UNE-EN 12350-2 (33), and air content and fresh density testing according to UNE-EN 12350-7 (34). A compressive strength test was conducted at 7, 28, and 60 curing days according to UNE-EN 12390-3 (35). Volume instability was measured according to ASTM C490-04 (36) and ASTM C1038 (37) up to 150 curing days for samples exposed to two types of curing environments: inside a curing chamber (labeled CC) and submerged in water inside an oven at 60ºC (labeled SW).

3. RESULTS AND DISCUSSION

Figure 3 shows XRD scans of the raw LFS samples. As expected, the samples presented similar qualitative mineralogical compositions (silicates/aluminates of calcium and magnesium) owing to their common origin and similar chemical composition. This included hydraulic reactive phases such as β-C_2S and mayenite, which could provide cementing activity. The noted presence of periclase is very important because of the possible expansion issues that it can produce. Additionally, hydration

TABLE 3. Chemical composition of the raw materials used: cement and LFS, coarse and fine.

Oxides	CaO	SiO_2	Al_2O_3	Fe_2O_3	SO_3	MgO	MnO	TiO_2	Cr_2O_3	Ca/Si	Si/Al	∑ others	LOI
CEM	63.2	18.7	4.0	3.3	2.9	1.4	0.0	0.2	0.0	3.4	4.7	1.2	5.0
LFS-G	45.6	19.3	6.7	10.8	1.8	5.8	1.7	0.5	0.8	2.4	2.9	0.8	6.2
LFS-F	48.1	20.7	5.6	7.2	1.9	6.6	1.3	0.4	0.4	2.3	3.7	0.7	7.1

and carbonation products like portlandite, brucite, and calcite were present because of the weathering process undergone by the slags in the plant. Finally, several non-reactive phases, such as γ-C_2S, gehlenite, merwinite, and wüstite were observed. The phases identified in the slags were in agreement with expectations from the literature (8, 30, 38), and it can be concluded that the milling process of the slag to obtain a finer PSD did not affect its mineralogical composition.

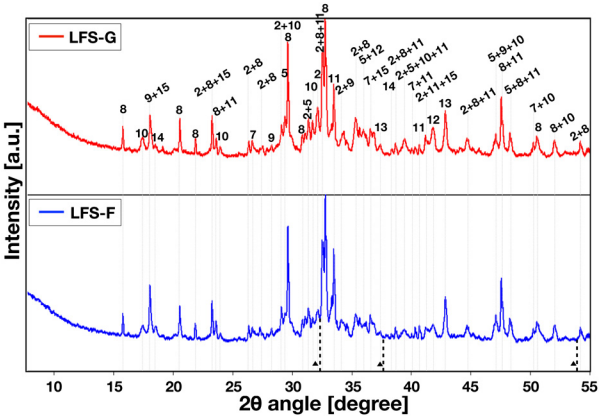

FIGURE 3. XRD diffractograms of as-received LFS-G and LFS-F samples with characteristic CaO peaks (dotted black lines), where annotations indicate: (2) β-C_2S; (5) calcite; (7) quartz; (8) γ-C_2S; (9) portlandite; (10) gehlenite; (11) merwinite; (12) wüstite; (13) periclase; (14) brucite; (15) mayenite; and (▲) free CaO.

Notably, an absence of free CaO was observed in both LFS samples, as there was no signal at its principal reflections (indicated in Figure 3 by a black triangle (▲) and segmented black lines). This is significant because this phase, if present, has potential to produce volumetric instability problems.

Figure 4 shows the ATR-FTIR results for the raw slags. The samples' spectra were very similar, showing differences only in certain peak intensities. They exhibited typical LFS phases, corroborating the XRD results. Some characteristic features due to the vibrations of Si–O and Al–O bonds (39, 40) formed a wide absorption band between 800 and 1100 cm^{-1} by virtue of overlapping C_2S polymorphs and the presence of merwinite/gehlenite/mayenite. Another band around 500 cm^{-1} with shoulders toward higher and lower wavenumbers was related to the presence of merwinite (39, 40) and wüstite (41) phases in the slags.

The presence of calcite was also evident from the characteristic bands around 1500 cm^{-1} and above 1000 cm^{-1}, which arise from different C–O bond vibration modes (42). The latter band shows a minor displacement and broadening toward higher wavenumbers that could be related to the vibration of Mg–O bonds in periclase/brucite (39, 43). At higher wavenumbers, it is worth noticing the peaks located around 3640 and 3700 cm^{-1}, which are due to the stretching vibration of the OH group present in portlandite (10, 38) and brucite (10, 39, 40), respectively. A peak that could not be unambiguously identified appeared between these peaks. This is thought to be related to a phase in the AFm/calcium aluminate hydrate family. Finally, a well-defined feature at 1630 cm^{-1} and a broader band in the baseline around 3500 cm^{-1}. These two features are characteristic of the OH group in water from the hydrated components of LFS (39, 44, 45). The absence of free CaO and the presence of periclase observed in the XRD results, along with the presence of brucite confirmed by the FTIR results, demonstrates that LFS experiences a maturity/weathering process, eliminating some of the problematic phases such as free CaO and part of the periclase.

Figure 5 and Figure 6 show the XRD scans of the hydrated LFS–concrete system (HG and HF, respectively) at 7, 28, 60, and 150 days. The slags showed

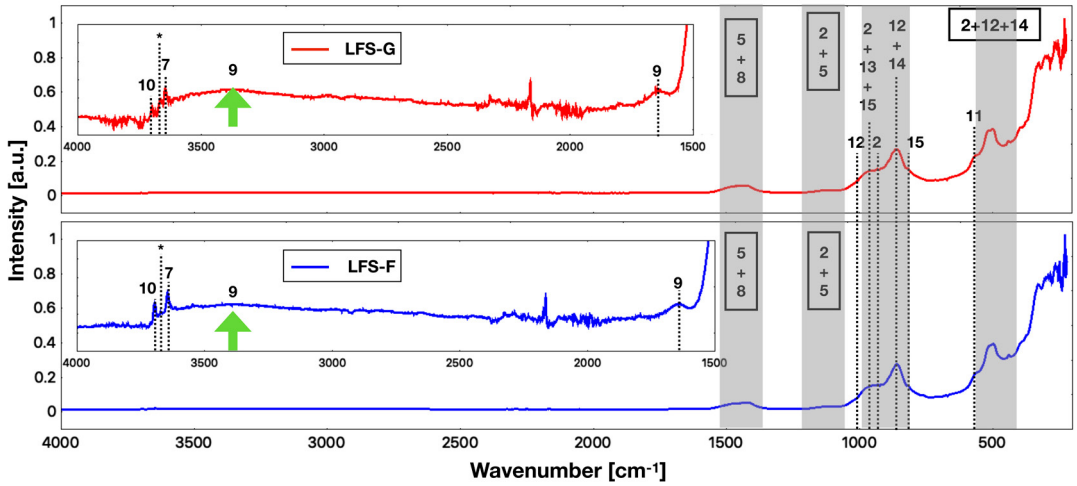

FIGURE 4. ATR-FTIR spectra of as-received LFS-G and LFS-F samples, where annotations indicate: (2) β-C_2S; (5) calcite; (7) portlandite; (8) periclase; (9) C-S-H gel; (10) brucite; (11) wüstite; (12) merwinite; (13) gehlenite; (14) mayenite; and (15) γ-C_2S.

similar mineralogical compositions and evolutions compared with the control sample. Initially, a combination of cement and LFS phases appeared, with the dilution effect of the minor components. This was observed as the main reflections tended to diminish or even disappear, in some cases. Then, as time passed and hydration occurred, the formation of typical concrete matrix products was observed.

At an early curing age, the characteristic reflections of crystalline phases in ordinary Portland cement concrete were exhibited owing to the hydration/carbonation process, such as portlandite (CH), ettringite (AFt), and calcite. Additionally, a decrease in the main C_3S and C_3A peaks was observed, together with total gypsum consumption. As time passed, there was a slight additional increase in the characteristic peaks of the hydration/carbonation products, especially those of calcite. At later ages, the formation of carboaluminate (AFm–CO_3) was observed. It was accompanied by a small decrease in the main reflection of calcite, which can be attributed to the transformation of AFt/AFm phases into AFm–CO_3. There was no sign of periclase consumption at early curing ages. Only in the final step, from 60 to 150 days in the CC environment, was there an apparent decrease in the main peak's intensity. On the other hand, the spectra at 150 days in the SW environment showed greater periclase consumption (i.e., a greater decrease in the main peak's intensity) due to an acceleration of the reactions under these conditions, along with an increase in brucite's main reflections. Finally, the characteristic peaks of phases in the anhydrous cement and non-reactive phases in LFS remained visible after 150 curing days in both environments. It should be noted that the HG and HF samples displayed a sort of displacement of the baseline in the form of a hump visible between 25º2θ and 40º2θ. This XRD signal is characteristic of C-S-H gel formed during the hydration reactions of LFS–concrete systems.

Figure 7 and Figure 8 show the ATR-FTIR spectra of hydrated LFS–concrete systems (HG and HF, respectively) at 7, 28, and 60 days. Both samples exhibited the typical crystalline phase formation of CH, AFt/AFm, and calcite, corroborating the XRD results. Furthermore, the formation of non-crystalline phases such as C-S-H gel (peaks marked with X) was clearly observed. This included a broad peak in the baseline around 3400 cm^{-1} and a well-defined peak at 1630 cm^{-1} related to the OH group from the chemically bonded water present in the amorphous C-S-H gel phase. Furthermore, the enhancement of some noticeable bands/peaks around 1000 cm^{-1} and 500 cm^{-1} was related to Si–O vibration modes due to the hydration of C_3S and C_2S present in the cement and slag. Finally, the presence of brucite was detected by its characteristic peak around 3700 cm^{-1}, which occurs at higher frequencies than that of portlandite.

Table 4 summarizes the fresh-state properties of all samples. The LFS–concrete samples exhibited increased air content and decreased fresh density, possibly due to the higher porosity of the slags compared to fine aggregates and the lower density of the slags compared to cement. The HG sample showed the highest air content of all samples. This may have been due to its extra-fine aggregate replacement, which presents a higher porosity than F-Ag. Slump/consistency tests showed decreased workability for the HG sample but increased workability for the HF sample. This change in behavior could have been related to the different slag contents in the samples' respective replacements. HG with dual cement/fine aggregate replacement presented a higher total slag content, which could lead to higher water demand than in the control sample. The HF sample's increased workability could have been

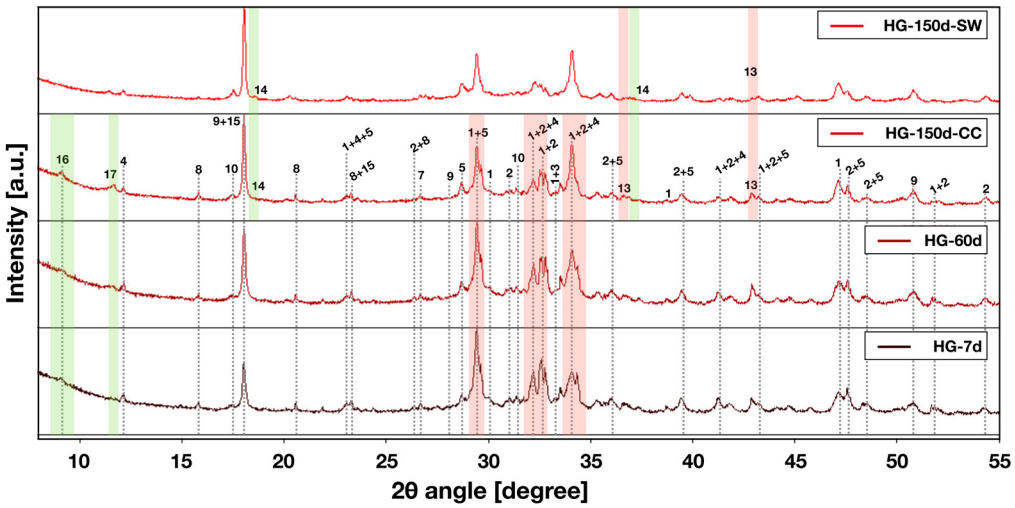

FIGURE 5. XRD diffractograms of HG at 7, 28, 60, and (for the samples exposed to two different curing environments only) 150 curing days, where annotations indicate: (1) C_3S; (2) β-C_2S; (3) C_3A; (4) C_4AF; (5) calcite; (7) quartz; (8) γ-C_2S; (9) portlandite; (10) gehlenite; (13) periclase; (14) brucite; (15) mayenite; (16) AFt; and (17) AFm–CO_3.

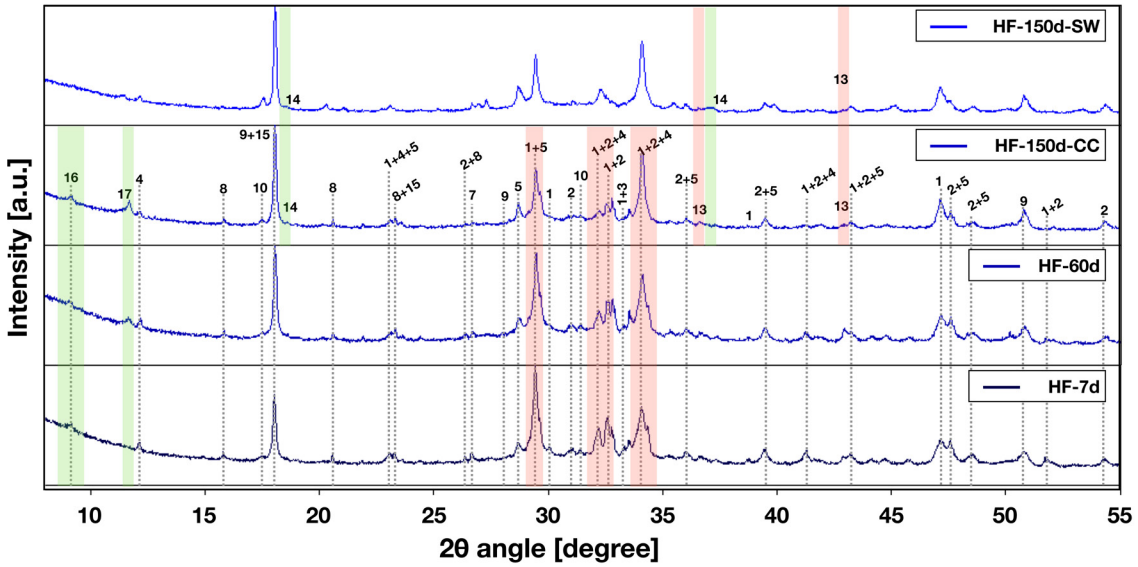

FIGURE 6. XRD diffractograms of HF at 7, 28, 60, and (for the samples exposed to two different curing environments only) 150 curing days, where annotations indicate: (1) C_3S; (2) β-C_2S; (3) C_3A; (4) C_4AF; (5) calcite; (7) quartz; (8) γ-C_2S; (9) portlandite; (10) gehlenite; (13) periclase; (14) brucite; (15) mayenite; (16) AFt; and (17) AFm–CO_3.

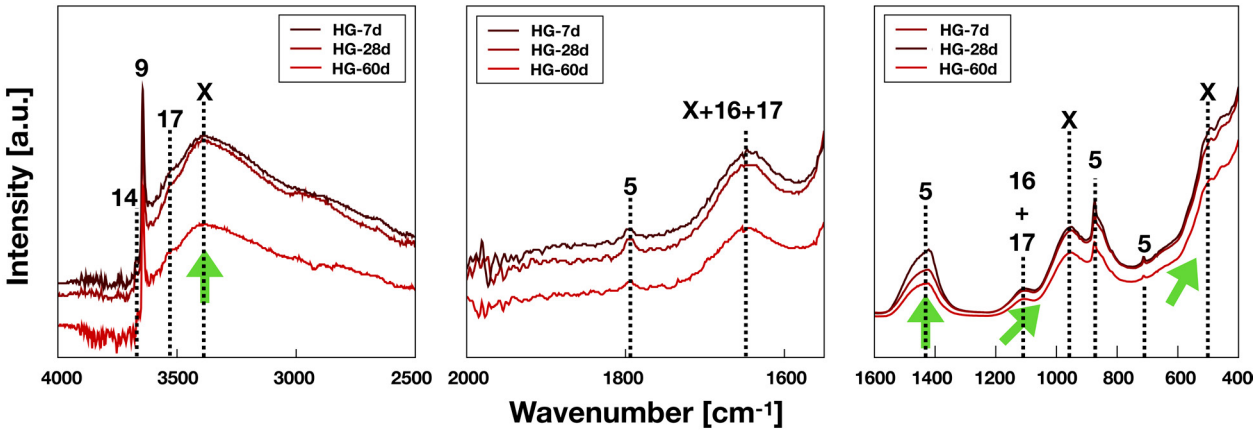

FIGURE 7. ATR-FTIR spectra of HG at 7, 28, and 60 curing days, where annotations indicate: (X) C-S-H gel; (5) calcite; (9) portlandite; (14) brucite; (16) AFt; and (17) AFm.

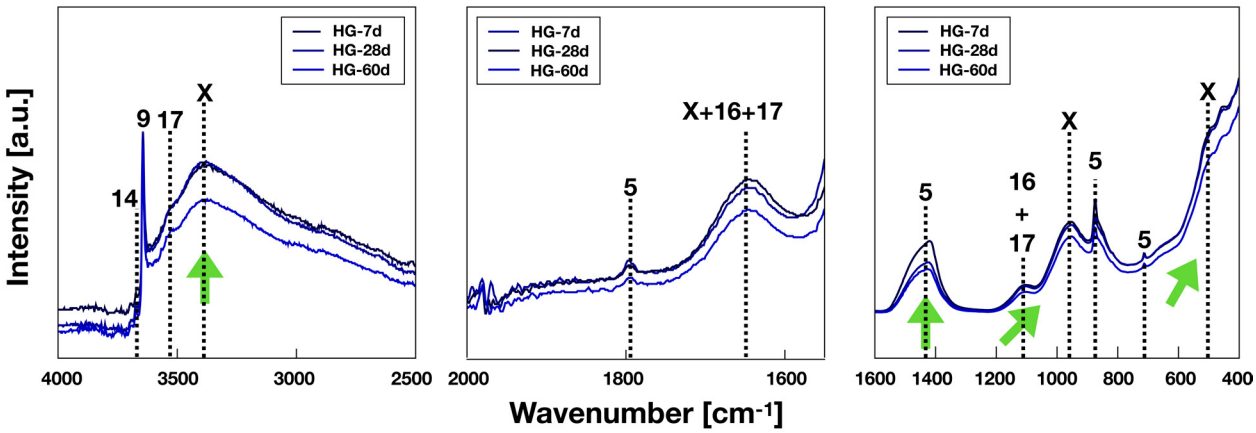

FIGURE 8. ATR-FTIR spectra of HF at 7, 28, and 60 curing days, where annotations indicate: (X) C-S-H gel; (5) calcite; (9) portlandite; (14) brucite; (16) AFt; and (17) AFm.

Table 4. Fresh-state properties of the concrete samples.

Sample	Air content (%)	Slump (cm)	Consistency	Fresh density (g/cm³)
HC	3.5	12	Fluid	2.42
HG	4.5	10	Fluid	2.37
HF	4.0	18	Liquid	2.38

related to its higher cement dilution effect due to the slag replacement and relatively greater availability of water and superplasticizer for reacting with cement.

Figure 9 shows the evolution of hardened-state properties at 7, 28, and 60 curing days. Density and compressive strength increased with time; in contrast, pore volume decreased. This behavior was expected because of the volume changes that accompany hydration, with newly formed products occupying previously free space. Consequently, the strength capacity of the material increased. Figure 9(a) shows that, for all samples, densities were in the range of 2.25 to 2.35 g/cm³, which was within the expected values. HG had the lowest density owing to its greater cement/filler dilution effect. HF presented higher density than the HG sample (i.e., closer to that of the control sample). This was probably because of a weaker cement dilution effect and better concrete compaction, as this sample exhibited higher workability (liquid consistency) and lower air content in the fresh state (see Table 4).

Figure 9(c) shows the compressive strength results for all samples. HC realized the best performance, with strength values of 49.4 MPa, 55.0 MPa, and 62.0 MPa at 7, 28, and 60 days, respectively. LFS–concrete samples displayed decreased strength compared to the control sample, with index performance rates of 74–81% and 58–65% for HG and HF, respectively (see Table 5). The reduced mechanical performance observed was mainly due to the cement dilution effect caused by the slag replacement and the lower cementing activity of the slag phases compared to Portland cement. Comparing the LFS concrete samples, HG presented better mechanical performance than HF at early curing ages, mostly due to a weaker dilution effect (with cement replacement of 18 wt% for HG and 24 wt% for HF). However, at later ages, this difference decreased owing to the contribution to the hydration process of β-C_2S, a slower-reacting phase with cementing activity present in cement and in both slags. However, as LFS-F had a lower PSD, its contribution was higher because of its higher specific surface area and hence the higher reactivity of the finer slag. Nonetheless, despite showing mechanical performance inferior to that of the control sample, both LFS-F and LFS-G attained compressive strength values of over 30 MPa at seven days and as high as 46 MPa at 60 days. This would allow these materials to be used in various applications; possibly, even as a structural material.

Figure 10 shows the volumetric instability behavior of concrete samples subjected for 150 days to two types of curing environments: inside a curing chamber (CC) and submerged in water inside an oven at 60ºC (SW). As observed in Figure 10(a), all samples subjected to the CC environment displayed a similar expansion tendency, reaching maximum values of approximately 0.02% during the controlled time. As all CC samples exhibited similar behavior, this could be related to a swelling effect due to the limited evaporation and moisture loss in this environment, thereby avoiding any shrinkage.

In the SW environment (Figure 10(b)), all samples showed an expansion tendency. HG and HF samples exhibited maximum expansion values of 0.028% and 0.025%, respectively. Reaching higher values than the control sample with only a maximum expansion val-

Table 5. Compressive strength index values of the concrete samples.

Sample	Compressive Strength Index (%)		
	7 d	28 d	60 d
HC	-	-	-
HG	81	77	74
HF	62	58	65

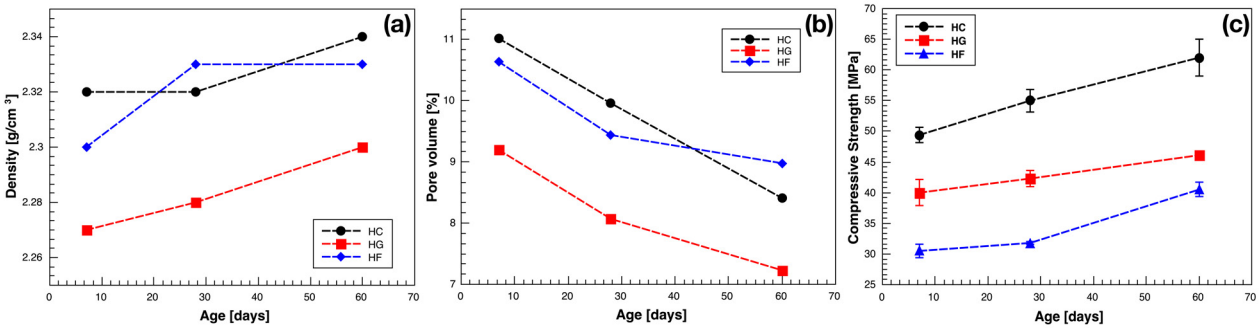

Figure 9. Hardened-state concrete properties for all samples: (a) density; (b) pore volume; and (c) compressive strength.

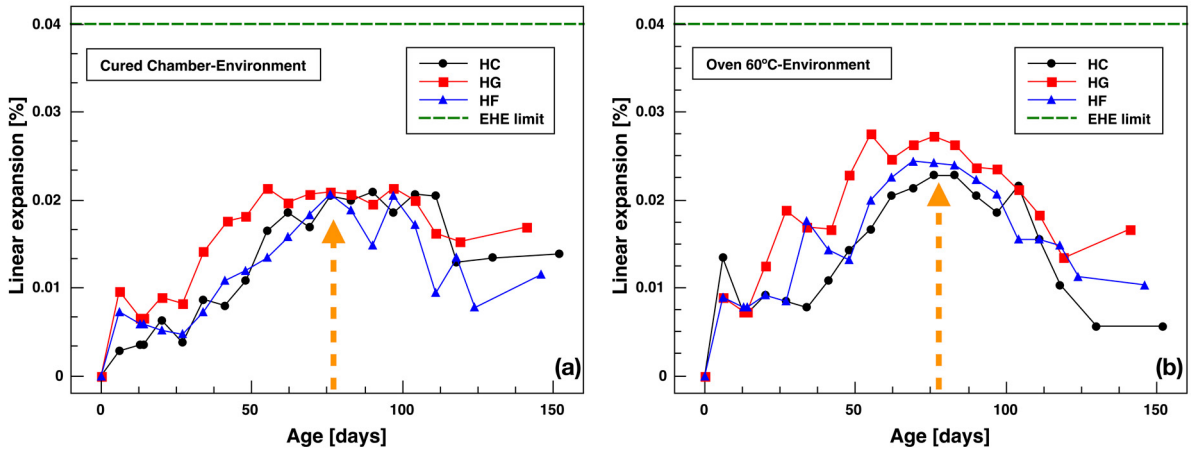

FIGURE 10. Volume instability results for samples subjected to two curing environments: (a) CC and (b) SW.

ue of 0.023%. This difference could be related to the activation of the remaining hydraulic and expansive phases present in LFS, such as β-C_2S, mayenite, and periclase. This type of environment may accelerate the hydration kinetics, starting to consume the remaining active phases. Comparing the mineralogical composition of the samples subjected to different curing environments, as in Figure 5 and Figure 6, the spectra of samples at 150 days were different for the SW environment. Diminished peaks related to periclase and slightly increased peaks associated with brucite (red and green zones, respectively) were evident, explaining the expansive behavior observed for both samples. The difference between HG and HF behavior, could be related to the greater total LFS content added and, consequently, the greater periclase content used as a replacement in the HG sample than in the HF sample: a total of 165.1 kg/m^3 instead of only 91.4 kg/m^3.

4. CONCLUSIONS

Our results suggest that using solely LFS as a dual cement/fine aggregate replacement or just as an SCM in concrete is feasible for both coarse and fine LFS. Results demonstrated volumetric instability within the established limits (0.04%) and acceptable mechanical performance. This finding could have significant environmental impact through reducing cement/aggregate consumption and recovering steel industry waste that would otherwise be deposited in landfills.

Mineralogical composition is a crucial factor in the performance of LFS as an SCM. In the absence of free CaO, special attention must be paid to the content and evolution of periclase because it is then the main phase responsible for expansive processes during hydration.

LFS–concrete samples exhibited reduced mechanical performance compared with the control sample. They also showed a dependence on content replacement at early curing ages, due mainly to the cement dilution effect. However, they reached non-negligible compressive strength values of 32–42 MPa at 28 curing days. At later curing ages, the presence of slowly reacting phases in the LFS contributed to increased strength while showing a dependence on PSD.

LFS–concrete samples exhibited volumetric instability problems; however, these were within the EHE established limits (0.04%). Since this instability increased in an accelerated curing environment, the remaining periclase could be responsible for the expansive behavior observed.

Special attention must be paid to the PSD and replacement content of an LFS when using it as a dual cement/aggregate replacement or just as an SCM. This could present an opportunity to lower the cost of the material (with no need to grind the slag), but may limit the maximum replacement content owing to potentially greater expansive behavior.

ACKNOWLEDGEMENTS

This work was supported by the National Agency for Research and Development (ANID) ex-CONICYT, DOCTORADO EN EL EXTRANJERO, BECAS CHILE/2019 – 72200568. Additionally, the authors would like to thank Adec Global for supplying the slag used in this research.

AUTHOR CONTRIBUTIONS:

Conceptualization: D. Aponte, M. Barra. Data curation: T. Montaño, P. Araos. Formal analysis: P. Araos, T. Montaño, D. Aponte. Funding acquisition: M. Barra, D. Aponte, S. Valls. Investigation: T. Montaño, P. Araos. Methodology: M. Barra, D. Aponte, S. Valls. Project administration: M. Barra, S. Valls. Resources: M. Barra, S. Valls. Software: P. Araos, D. Aponte. Supervision: M. Barra, D. Aponte. Validation. M. Barra, S. Valls. Visualization: P. Araos, T. Montaño. Writing, original draft: P. Araos. Writing, review & editing: P. Araos, D. Aponte.

REFERENCES

1. Schneider, M. (2019) The cement industry on the way to a low-carbon future. *Cem. Concr. Res.* 124, 105792. https://doi.org/10.1016/j.cemconres.2019.105792.
2. Madlool, N.A.; Saidur, R.; Rahim, N.A.; Kamalisarvestani, M. (2013) An overview of energy savings measures for cement industries. *Renew. Sust. Energ. Rev.* 19, 18-29. https://doi.org/10.1016/j.rser.2012.10.046.
3. Lothenbach, B.; Scrivener, K.; Hooton, R.D. (2011) Supplementary cementitious materials. *Cem. Concr. Res.* 41 [12], 1244-1256. https://doi.org/10.1016/j.cemconres.2010.12.001.
4. Thomas, M. (2013) Supplementary cementing materials in concrete, 1st ed., CRC Press, Boca Raton. https://doi.org/10.1201/b14493.
5. Pauliuk, S.; Milford, R.L.; Müller, D.B.; Allwood, J.M. (2013) The steel scrap age. *Environ. Sci. Technol.* 47 [7], 3448-3454. https://doi.org/10.1021/es303149z.
6. Montenegro-Cooper, J.M.; Celemín-Matachana, M.; Cañizal, J.; González, J.J. (2019) Study of the expansive behavior of ladle furnace slag and its mixture with low quality natural soils. *Constr. Build. Mater.* 203, 201-209. https://doi.org/10.1016/j.conbuildmat.2019.01.040.
7. Adesanya, E.; Sreenivasan, H.; Kantola, A.M.; Telkki, V.V.; Ohenoja, K.; Kinnunen, P.; et. al. (2018) Ladle slag cement - Characterization of hydration and conversion. *Constr. Build. Mater.* 193, 128-134. https://doi.org/10.1016/j.conbuildmat.2018.10.179.
8. Wang, Y.; Suraneni, P. (2019) Experimental methods to determine the feasibility of steel slags as supplementary cementitious materials. *Constr. Build. Mater.* 204, 458-467. https://doi.org/10.1016/j.conbuildmat.2019.01.196.
9. Ranfionich, E.V.; Barra, M. (2001) Reactividad y expansión de las escorias de acería de horno de arco eléctrico en relación con sus aplicaciones en la construcción. *Mater. Construcc.* 51 [263-264], 137-148. https://doi.org/10.3989/mc.2001.v51.i263-264.359.
10. Setién, J.; Hernández, D.; González, J.J. (2009) Characterization of ladle furnace basic slag for use as a construction material. *Constr. Build. Mater.* 23 [5], 1788-1794. https://doi.org/10.1016/j.conbuildmat.2008.10.003.
11. Yildirim, I.Z.; Prezzi, M. (2011) Chemical, mineralogical, and morphological properties of steel slag. *Adv. Civ. Eng.* 2011, 463638. https://doi.org/10.1155/2011/463638.
12. Montenegro, J.M.; Celemín-Matachana, M.; Cañizal, J.; Setién, J. (2013) Ladle furnace slag in the construction of embankments: expansive behavior. *J. Mater. Civ. Eng.* 25 [8], 972-979. https://doi.org/10.1061/(ASCE)MT.1943-5533.0000642.
13. Shi, C. (2004) Steel slag—its production, processing, characteristics, and cementitious properties. *J. Mater. Civ. Eng.* 16 [3], 230-236. https://doi.org/10.1061/(ASCE)0899-1561(2004)16:3(230).
14. Papayianni, I.; Anastasiou, E. (2012) Effect of granulometry on cementitious properties of ladle furnace slag. *Cem. Concr. Compos.* 34 [3], 400-407. https://doi.org/10.1016/j.cemconcomp.2011.11.015.
15. Choi, S.; Kim, J. (2020) Hydration reactivity of calcium-aluminate-based ladle furnace slag powder according to various cooling conditions. *Cem. Concr. Compos.* 114, 103734. https://doi.org/10.1016/j.cemconcomp.2020.103734.
16. Zhao, J.; Liu, Q.; Fang, K. (2020) Optimization of f-MgO/f-CaO phase in ladle furnace slag by air rapidly cooling. Mater. Lett. 280, 128528. https://doi.org/10.1016/j.matlet.2020.128528.
17. Tossavainen, M.; Engstrom, F.; Yang, Q.; Menad, N.; Lidstrom Larsson, M.; Bjorkman, B. (2007) Characteristics of steel slag under different cooling conditions. *Waste Manag.* 27 [10], 1335-1344. https://doi.org/10.1016/j.wasman.2006.08.002.
18. Adolfsson, D.; Robinson, R.; Engström, F.; Björkman, B. (2011) Influence of mineralogy on the hydraulic properties of ladle slag. *Cem. Concr. Res.* 41 [8], 865-871. https://doi.org/10.1016/j.cemconres.2011.04.003.
19. Herrero, T.; Vegas, I.J.; Santamaría, A.; San-José, J.T.; Skaf, M. (2016) Effect of high-alumina ladle furnace slag as cement substitution in masonry mortars. *Constr. Build. Mater.* 123, 404-413. https://doi.org/10.1016/j.conbuildmat.2016.07.014.
20. Rodríguez, A.; Santamaría-Vicario, I.; Calderón, V.; Junco, C.; García-Cuadrado, J. (2019) Study of the expansion of cement mortars manufactured with Ladle Furnace Slag LFS. *Mater. Construcc.* 69 [334], e183. https://doi.org/10.3989/mc.2019.06018.
21. Sideris, K.K.; Tassos, C.; Chatzopoulos, A.; Manita, P. (2018) Mechanical characteristics and durability of self compacting concretes produced with ladle furnace slag. *Constr. Build. Mater.* 170, 660-667. https://doi.org/10.1016/j.conbuildmat.2018.03.091.
22. Anastasiou, E.K.; Papayianni, I.; Papachristoforou, M. (2014) Behavior of self compacting concrete containing ladle furnace slag and steel fiber reinforcement. *Mater. Des.* 59, 454–460. https://doi.org/10.1016/j.matdes.2014.03.030.
23. Papayianni, I.; Anastasiou, E. (2010) Production of high-strength concrete using high volume of industrial by-products. *Constr. Build. Mater.* 24 [8], 1412–1417. https://doi.org/10.1016/j.conbuildmat.2010.01.016.
24. Sadiqul Islam, G.M.; Akter, S.; Reza, T.B. (2022) Sustainable high-performance, self-compacting concrete using ladle slag. *Clean. Eng. Technol.* 7, 100439. https://doi.org/10.1016/j.clet.2022.100439.
25. Santamaría, A.; González, J.J.; Losáñez, M.M.; Scaf, M.; Ortega-López, V. (2020) The design of self-compacting structural mortar containing steelmaking slag as aggregate. *Cem. Concr. Compos.* 111, 103627. https://doi.org/10.1016/j.cemconcomp.2020.103627.
26. Ortega-López, V.; García-Llona, A.; Revilla-Cuesta, V.; Santamaría, A.; San-Jose, J.T. (2021) Fiber-reinforcement and its effects on the mechanical properties of high-workability concretes manufactured with slag as aggregate and binder. *J. Build. Eng.* 43, 102548. https://doi.org/10.1016/j.jobe.2021.102548.
27. UNE-EN 197-1, Cement - Part 1: Composition, specifications and conformity criteria for common cements. AENOR, Madrid, 2011.
28. UNE-EN 933-1, Tests for geometrical properties of aggregates - Part 1: Determination of particle size distribution - Sieving method. AENOR, Madrid, 2012.
29. UNE 80103, Test methods of cements. Physical analysis. Actual density determination. AENOR, Madrid, 2013.
30. Yi, H.; Xu, G.; Cheng, H.; Wang, J.; Wan, Y.; Chen, H. (2013) An overview of utilization of steel slag. *Procedia Environ. Sci.* 16, 791–801. https://doi.org/10.1016/j.proenv.2012.10.108.
31. Adolfsson, D.; Engström, F.; Robinson, R.; Björkman, B. (2010) Cementitious phases in ladle slag. *Steel Res. Int.* 82 [4], 398–403. https://doi.org/10.1002/srin.201000176.
32. Saez-de-Guinoa Vilaplana, A.; Ferreira, V.J.; López-Sabirón, A.M.; Aranda-Usón, A.; Lausín-González, C.; Berganza-Conde, C.; et al. (2015) Utilization of ladle furnace slag from a steelwork for laboratory scale production of portland cement. *Constr. Build. Mater.* 94, 837–843. https://doi.org/10.1016/j.conbuildmat.2015.07.075.
33. UNE-EN 12350-2. (2020) Testing fresh concrete – Part 2: Slump test. AENOR, Madrid.
34. UNE-EN 12350-7. (2020) Testing fresh concrete – Part 7: Air content – pressure methods. AENOR, Madrid.
35. UNE-EN 12390-3. (2020) Testing hardened concrete – Part 3: Compressive strength of test specimens. AENOR, Madrid.
36. ASTM C490 / C490M-17 (2017) Standard practice for use of apparatus for the determination of length change of hardened cement paste, mortar, and concrete. ASTM International, West Conshohocken, PA.
37. ASTM C1038 / C1038M-19. (2019) Standard test method for expansion of hydraulic cement mortar bars stored in water. ASTM International, West Conshohocken, PA. https://doi.org/10.1520/C0109_C0109M.
38. Rađenović, A.; Malina, J.; Sofilić, T. (2013) Characterization of ladle furnace slag from carbon steel production as a potential adsorbent. *Adv. Mater. Sci. Eng.* 2013, 1-6. https://doi.org/10.1155/2013/198240.
39. Hughes, T.L.; Methven, C.M.; Jones, T.G.J.; Pelham, S.E.; Fletcher, P.; Hall, C. (1995) Determining cement composition by Fourier transform infrared spectroscopy. *Adv. Cem.*

Based Mater. 2 [3], 91-104. https://doi.org/10.1016/1065-7355(94)00031-X.
40. Horgnies, M.; Chen, J.J.; Bouillon, C. (2013) Overview about the use of fourier transform infrared spectroscopy to study cementitious materials. in: Mc13, WIT Press, Southampton, UK, 251-262. https://doi.org/10.2495/MC130221.
41. Kriskova, L.; Pontikes, Y.; Cizer, Ö.; Malfliet, A.; Dijkmans, J.; Sels, B.; et al. (2014) Hydraulic Behavior of mechanically and chemically activated synthetic merwinite. *J. Am. Ceram. Soc.* 97 [12], 3973–3981. https://doi.org/10.1111/jace.13221.
42. Li, J.; Yu, Q.; Wei, J.; Zhang, T. (2011) Structural characteristics and hydration kinetics of modified steel slag. *Cem. Concr. Res.* 41 [3], 324-329. https://doi.org/10.1016/j.cemconres.2010.11.018.
43. Fernández-Carrasco, L.; Torrens-Martín, D.; Morales, L.M.; Martínez-Ramírez, S. (2012) Infrared spectroscopy in the analysis of building and construction materials. T. Theophanides (Ed.), Infrared spectroscopy - materials science, engineering and technology, InTech. 369-382. https://doi.org/10.5772/36186.
44. Kriskova, L.; Pontikes, Y.; Cizer, Ö.; Mertens, G.; Veulemans, W.; Geysen, D.; et al. (2012) Effect of mechanical activation on the hydraulic properties of stainless steel slags. *Cem. Concr. Res.* 42 [6], 778-788. https://doi.org/10.1016/j.cemconres.2012.02.016.
45. Kuenzel, C.; Zhang, F.; Ferrándiz-Mas, V.; Cheeseman, C.R.; Gartner, E.M. (2018) The mechanism of hydration of MgO-hydromagnesite blends. *Cem. Concr. Res.* 103, 123-129. https://doi.org/10.1016/j.cemconres.2017.10.003.